remote sensing

MDPI

Article

Seismic Interferometry for Single-Channel Data: A Promising Approach for Improved Offshore Wind Farm Evaluation

Rui Wang [1], Bin Hu [2], Hairong Zhang [1,*], Peizhen Zhang [1], Canping Li [1] and Fengying Chen [1]

[1] College of Electronic and Information Engineering, Guangdong Ocean University, Zhanjiang 524088, China; wangrui@gdou.edu.cn (R.W.); zhangpz@gdou.edu.cn (P.Z.); licp@gdou.edu.cn (C.L.); chenfy@gdou.edu.cn (F.C.)
[2] College of Geo-Exploration Science and Technology, Jilin University, Changchun 130026, China; binhu@jlu.edu.cn
* Correspondence: zhanghr1985@gdou.edu.cn

Abstract: Single-channel seismic (SCS) methods play a crucial role in offshore wind farm assessments, offering rapid and continuous imaging of the subsurface. Conventional SCS methods often fall short in resolution and signal completeness, leading to potential misinterpretations of geological structures. In this study, we propose the application of seismic interferometry as a powerful tool to address these challenges by utilizing multiple reflections that are usually considered as noise. First, we demonstrate the feasibility of using seismic interferometry to approximate the primary wavefield. Then, we evaluate a series of seismic interferometry applied in SCS data, including cross-correlation, deconvolution, and cross-coherence, and determine the most appropriate one for our purpose. Finally, by comparing and analyzing the differences in amplitude, continuity, time–frequency properties, etc., between conventional primary wavefield information and reconstructed primary wavefield information by seismic interferometry, it is proved that incorporating multiples as supplementary information through seismic interferometry significantly enhances data reliability and resolution. The introduction of seismic interferometry provides a more detailed and accurate geological assessment crucial for optimal site selection in offshore wind farm development.

Keywords: offshore wind farm; single-channel seismic (SCS); seismic interferometry; multiple reflection; high resolution

check for updates

Academic Editors: Filippo Carboni, Maurizio Ercoli and Ramon Carbonell

Received: 22 November 2024
Revised: 14 January 2025
Accepted: 16 January 2025
Published: 17 January 2025

Citation: Wang, R.; Hu, B.; Zhang, H.; Zhang, P.; Li, C.; Chen, F. Seismic Interferometry for Single-Channel Data: A Promising Approach for Improved Offshore Wind Farm Evaluation. *Remote Sens.* **2025**, *17*, 325. https://doi.org/10.3390/rs17020325

Copyright: © 2025 by the authors. Licensee MDPI, Basel, Switzerland. This article is an open access article distributed under the terms and conditions of the Creative Commons Attribution (CC BY) license (https://creativecommons.org/licenses/by/4.0/).

1. Introduction

Offshore wind power is environmentally friendly and can provide a sustainable energy supply, which has become a key component in the development of renewable energy globally [1]. The accurate evaluation of offshore wind farm sites is essential for guaranteeing the safety and stability of these installations because high-quality assessments can effectively prevent issues such as foundation settlement caused by geological instability [2]. Traditional site assessments for offshore wind farms depend heavily on drilling methods [3], which, while providing precise geological data at depth, are costly and time-consuming in regional surveys [4]. To overcome these shortcomings, the single-channel seismic (SCS) method has become an important technological addition to the site assessment, offering detailed subsurface images required to identify geological structures [5], which is called sub-bottom profiling [6]. SCS acquisition involves deploying a single hydrophone streamer and a sound source, both towed by a vessel to emit acoustic signals and record their reflection wavefield [7]. Compared with traditional drilling, this configuration of SCS

facilitates the continuous acquisition of seismic profiles along the survey track, which allows for continuous and rapid detection of bedrock distributions and shallow geological structures, greatly enhancing the efficiency and scope of exploration [8]. Until now, the SCS method has been successfully applied in offshore wind farms with encouraging results such as accurately mapping seabed conditions, identifying shallow geological features, and detecting potential geohazards such as buried channels and fault lines [3,9,10].

However, the application of the single-channel seismic method in offshore wind farm site assessments encounters certain limitations, particularly when facing challenging acquisition conditions due to the inherent inability of SCS to adopt Common Midpoint (CMP) stacking and the lack of multi-offset wavefield to improve signal-to-noise ratio and data quality [11]. These limitations can lead to distorted or incomplete recorded profiles, which might be mistakenly interpreted as geological structures, thereby reducing the reliability of site assessments. Moreover, in the context of joint drilling-seismic interpretation, the SCS method still falls short of achieving the drilling-like high resolution [12,13]. This deficiency in resolution increases the likelihood of errors when defining geological structures during site assessments, potentially leading to poor choices in site selection decisions [14,15].

In recent years, the rapid development of seismic interferometry has offered new possibilities for overcoming these challenges of incomplete signal and resolution deficiency. It refers to a kind of data-driven methods that transform recorded signal or noise into target signal through cross-correlation, deconvolution, or cross-coherence [16–20]. Utilizing this property, many wavefields typically regarded as unexpected interference in conventional processing, such as ambient noise, surface waves, and multiple reflections, can be used as supplemental information to enhance imaging completeness and resolution [21,22]. Recent research has demonstrated its exceptional performance in various fields of geoscience. For instance, Qiao et al. have effectively enhanced reflection signals, achieving high-quality near-surface imaging [23], while Huang et al. have applied seismic interferometry in core studies, achieving high-precision detection of the Earth's core [22].

Despite these advances, improving the reliability of offshore wind farm assessment using seismic interferometry still faces many challenges [24] due to the low signal-to-noise ratio of SCS data [25] and the constrained spatial coverage of the associated wavefield information [26]; however, seismic interferometry relies on signal coherence to reconstruct virtual source wavefields [20], insufficient wavefield information may lead to insufficient signal coherence during the interferometry process, resulting in a significant decrease in the quality of the reconstruction results.

Considering the propagation conditions in the ocean, multiple reflections are typically considered common noise, which is strongly coherent with the primaries. Boullenger and Draganov utilized seismic interferometry to transform multiple reflections into effective information, enhancing the primaries and revealing small-scale geological features [27,28]. The addition of multiple illuminates underground areas that are difficult to reach with primary inverts near-surface information improves the signal-to-noise ratio of complex images and achieves sub-wavelength imaging, etc. [29,30]. These advantages mean that multiple is a valuable supplementary choice for the interferometry process in SCS data.

Furthermore, previous studies demonstrate that different seismic interferometry techniques (such as cross-correlation, deconvolution, and cross-coherence) perform well under specific noise conditions. For instance, cross-coherence is less sensitive to shallow source noise, whereas cross-correlation and deconvolution are less affected by source bandwidth, offering higher resolution [31]. The suitability of seismic interferometry also varies with different observational systems, such as when overlaying weathered layers or in inter-well VSP scenarios [32]. These insights indicate that the application of traditional interferome-

try methods to SCS data necessitates further investigation to determine feasibility, refine interferometric algorithms, and select appropriate wavefield components.

Therefore, in this paper, we treat multiples as supplementary information in seismic interferometry to explore how to obtain high-quality offshore wind farm site assessment results. To obtain the best interferometry results, we analyze and select the effectiveness of different interferometry methods applied to offshore wind farm data. The experimental results show that the deconvolution method has advantages in signal-to-noise ratio and resolution and is more suitable for wind farm seismic data. By comparing the interferometry results with conventional processing outcomes, we objectively evaluate the strengths and weaknesses of both approaches and propose how to utilize them to achieve optimal site assessment results.

This paper is structured as follows: In Section 2, we review the basic principles of seismic interferometry and elucidate the propagation relationships of primaries and multiple reflections, theoretically justifying the feasibility of constructing quasi-primary wavefields via seismic interferometry. We present the SCS field data and the processing workflow to obtain primaries. In Section 3 we compare the different interferometric algorithms, including cross-correlation, deconvolution, and cross-coherence algorithms, to select the most suitable processing approach for SCS data. In Section 4, we evaluate the new processing workflow's application potential and future development directions. In Section 5, we state the conclusion and prospect of this paper.

2. Materials and Methods

2.1. Review of Seismic Interferometry

In the field of seismic exploration, there is a method called seismic interferometry that can use the travel time and phase difference of seismic signals to obtain the propagation characteristics of the underground medium. This method allows for the construction of virtual signals between any two seismic traces without the need for detailed prior information (i.e., transforming the seismic signals received by two receivers into a signal that appears to be emitted at one receiver and received at the other, as shown in Figure 1). By utilizing seismic interferometry to reconstruct recorded seismic data, it is possible to circumvent overburden layers, focusing the reconstructed wavefield within the target area. This targeted approach enables geological structure imaging of the object of interest, thus avoiding interference from complex overlying layers and enhancing imaging accuracy.

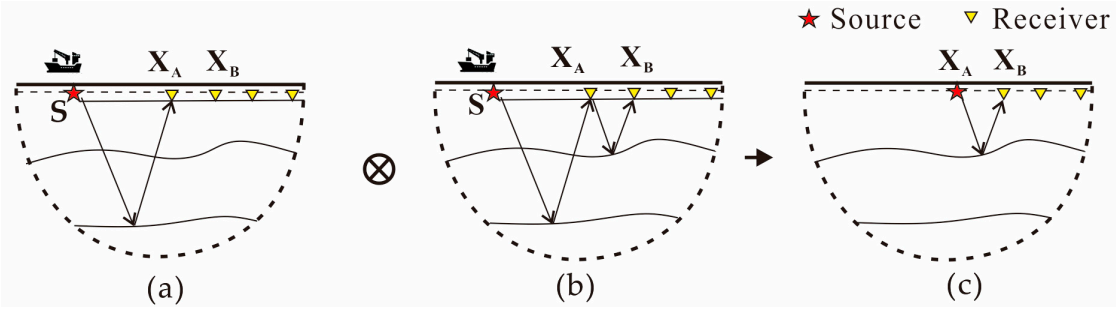


Figure 1. Schematic diagram of seismic interferometry. This process can be understood simply as the seismic interferometry technique being able to cancel the overlapping paths between two seismic waves (**a**,**b**) and to construct a new signal (**c**).

In seismic interferometry, seismic records are considered as the convolution of Green's function with the seismic wavelet, indicating that solving for Green's function of the virtual source records is the key issue in seismic interferometry. In a 3D acoustic medium, Green's

function can be regarded as the response to a point impulse from source S to receiver x_A. In the frequency domain, Green's function must satisfy the Helmholtz equation,

$$(\nabla^2 + k^2)G(x_A, S) = -\delta(S - x_A), \tag{1}$$

where $k = \omega/v$ is the wavenumber and v is the medium velocity. Green's function can be solved as

$$G(x_A, S) = \frac{1}{4\pi}\frac{e^{ikr}}{r}, \tag{2}$$

where $r = |x_A - S|$, $1/r$ means geometric spreading and $e^{-i\omega t}$ represents the inverse Fourier transform.

For an acoustic medium, Green's function can represent the primary parameters of the seismic wavefield, namely the pressure field p and the particle velocity v; the equations are given as follows:

$$p(x, \omega) = G(x, x_{\mathrm{A}}, \omega), \tag{3}$$

$$v_{i,A}(x, \omega) = -(j\omega\rho(x))^{-1}G(x, x_A, \omega), \tag{4}$$

where $\rho(x)$ represents the density of the medium. Using the pressure field and particle velocity, the stress–strain relationship in the acoustic medium can be further constructed:

$$\hat{f}_i = j\omega\rho v_i + \partial_i p, \tag{5}$$

$$\hat{u} = j\omega\kappa p + \partial_i v_i, \tag{6}$$

where $\hat{f}_i$ represents the external volumetric force density, S denotes the source field quantity, and $\kappa(x)$ represents the bulk modulus.

Substituting Equations (3)–(6) into the reciprocity theorem for an acoustic medium, as shown in Equation (7):

$$\begin{aligned} &\int_D \Big\{ p_A(x,\omega)S(x,\omega) + v_{i,A}(x,\omega)\hat{f}_{i,B}(x,\omega) \\ &+S(x,\omega)\hat{p}_B(x,\omega) + \hat{f}_{i,B}(x,\omega)v_{i,B}(x,\omega) \Big\} d^3x \\ &= \oint_{\partial D} \{\hat{p}_A(x,\omega)v_{i,B}(x,\omega) + v_{i,A}(x,\omega)\hat{p}_B(x,\omega)\} n_i d^2x \end{aligned} \quad , \tag{7}$$

The seismic interferometry equation can be derived as:

$$\begin{aligned} &2R\{\hat{G}(x_A, x_B, \omega) = \\ &\oint_{\partial D} \frac{-1}{j\omega\rho(x)} \{\hat{G}^*(x_A, x, \omega)\partial_i \hat{G}(x_B, x, \omega) - \partial_i \hat{G}(x_A, x, \omega)^* \hat{G}(x_B, x, \omega)\} n_i d^2x \end{aligned} \quad , \tag{8}$$

where R represents the "real part," $\hat{G}(x_{(\mathrm{A|B})}, x, \omega)$ indicating the response received at points x_A or x_B when the source is activated at location x.$\partial_i \hat{G}(x_{(\mathrm{A|B})}, x, \omega)n_i$ denotes the response received at points x_A or x_B when a dipole source is activated at location x. Furthermore, combining Equation (6) with Equation (8) allows simplification of the source-related parameters, and Equation (8) can be rewritten as:

$$\begin{aligned} G_c(x_B, x_A, \omega)\} &= u(x_B, S, \omega)u^*(x_A, S, \omega) \\ &= |W(S, \omega)|^2 G(x_B, S, \omega)G^*(x_A, S, \omega) \end{aligned} \quad , \tag{9}$$

where, $u(x_B, S, \omega) = W(S, \omega)G(x_B, S, \omega)$, represents the seismic signal received at the location x_B and excited at S; this can be understood as the product of the source wavelet $W(S, \omega)$ and Green's function $G(x_B, S, \omega)$. Seismic interferometry methods can mainly be categorized into three types: cross-correlation, deconvolution, and cross-coherence [33].

Among these interferometry methods, the cross-correlation method, which can be represented by Equation (9), is the most widely applied and is the most fundamental approach to seismic interferometry. Based on Equation (9), it is evident that the cross-correlation method directly calculates the correlation of seismic data. This process introduces the square of the source wavelet amplitude, which enhances the high-amplitude frequency components and weakens the low-amplitude ones, leading to a narrower effective frequency band of the computational results.

Correlation and deconvolution are closely related processes. The deconvolution method calculates the propagation effects between two detectors by deconvolving these data between them. Initially applied to well-log data processing [34], this method was later extended to seismic data processing [35]. For seismic wavefields excited at the source location S and received at two points x_A and x_B, the deconvolution seismic interferometry process can be represented by:

$$G_D(x_B, x_A, \omega)\} = \frac{u(x_\mathrm{B}, S, \omega)}{u(x_A, S, \omega)} = \frac{G(x_B, S, \omega)G^*(x_A, S, \omega)}{|G(x_B, S, \omega)|^2}. \tag{10}$$

From Equation (10), the deconvolution method eliminates the influence of the source wavelet by performing division in the frequency domain, which enhances the stability of the interferometry process. Furthermore, the amplitude information of each frequency is normalized, which broadens the effective frequency band of the results.

The cross-coherence-based seismic interferometry [36,37] can be written as follows:

$$G_H(x_B, x_A, \omega)\} = \frac{u(x_B, S, \omega)u^*(x_A, S, \omega)}{|u(x_B, S, \omega)||u(x_A, S, \omega)|}, \tag{11}$$

Similar to the deconvolution method, the coherence method broadens the effective frequency band but requires knowledge of the excitation's power spectrum to extract Green's function [38,39].

2.2. Retrieving Quasi-Primary by Seismic Interferometry

In this section, we will introduce the seismic interferometry process suited for offshore wind farm data. Initially, we review the propagation relation between primary and multiple. Then, we discuss how to integrate offshore wind farm data with seismic interferometry.

2.2.1. Multiple Model

Currently, the most widely used method for multiple model extraction is the Surface-Related Multiple Elimination (SRME) method [40], which is entirely data-driven and requires no subsurface medium information.

Assuming a plane wave propagates in a horizontally homogeneous velocity medium due to the strong reflective interface between air and seawater, the seismic wavefield will undergo multiple reflections. In theory, the prediction process of the 1D SRME algorithm is to convolution and sum these primary data and original data containing primary and multiple responses to obtain the predicted multiple models in a given integral interval. Its basic principle is as follows:

First, the source wavelet is defined as $s(t)$. The primary response of the stratum is $r(t)$. Then, the primary reflection response $p(t)$ can be expressed as:

$$p(t) = s(t) * r(t). \tag{12}$$

The primary reflection response propagates to the sea surface, and the reflection propagates downward, and then the first-order multiple response $m_1(t)$ is obtained by re-reflection of the stratum:

$$m_1(t) = r_0 p(t) * r(t) = r_0 s(t) * r(t) * r(t), \tag{13}$$

where r_0 represents the reflection coefficient. The sum of all multiple responses, that is, the multiple model, is:

$$\begin{aligned} m(t) &= m_1(t) + m_2(t) + \ldots + m_n(t) \\ &= s(t) * [r_0 r(t) + r_0^2 r(t) * r(t) + \ldots + r_0^n \underbrace{r(t) * r(t)}_{(n+1)}]. \end{aligned} \tag{14}$$

In the frequency domain, the primary response $P(\omega)$, whole multiple responses $M(\omega)$, and these full-wavefield data $D(\omega)$ can be represented as:

$$P(\omega) = W(S, \omega) R(\omega), \tag{15}$$

$$M(\omega) = W(S, \omega)\Big[r_0 R^2(\omega) + {r_0}^2 R^3(\omega) + \ldots + {r_0}^n R^{n+1}(\omega)\Big], \tag{16}$$

$$D(\omega) = W(S, \omega)\Big[R(\omega) + r_0 R^2(\omega) + {r_0}^2 R^3(\omega) + \ldots + {r_0}^n R^{n+1}(\omega)\Big], \tag{17}$$

where ω represents the angular frequency. We denote that $A^i(\omega) = \left[r_0 W(S, \omega)^{-1}\right]^i$, and then these full-wavefield data $D(\omega)$ and the whole multiple responses $M(\omega)$ can be written as the following series expansion:

$$M_i(\omega) = A^i(\omega) P(\omega)^{i+1}, \tag{18}$$

Therefore, in order to simplify the representation, we can express the primary $P(\omega)$ in the form of a 0th-order multiple, which is,

$$P(\omega) = A^0(\omega) P(\omega)^1 = M_0(\omega), \tag{19}$$

Thus, we can rewrite these full-wavefield data $D(\omega)$ as follows:

$$\begin{aligned} D(\omega) &= P(\omega) + A^1(\omega) P(\omega)^2 + A^2(\omega) P(\omega)^3 + \ldots + A^n(\omega) P(\omega)^{n+1} \\ &= M_0(\omega) \ + M_1(\omega) + M_2(\omega) + \ldots + M_n(\omega) \end{aligned}. \tag{20}$$

2.2.2. Retrieving Quasi-Primary by Multiple Reflection

As mentioned above, seismic interferometry requires two input datasets that share the same propagation paths. Offshore wind farm data mainly consist of primary and multiples, with multiples having propagation paths that significantly overlap with those of primary. This makes them well-suited as input data for interferometry; therefore, in single-channel seismic methods, seismic interferometry calculations between primary and multiples can transform multiples, which have wider propagation paths and carry more information, into quasi-primary signals. This approach provides more valuable information for wind farm site selection. The principle of this method is as follows: by combining Equations (12), (19), and (20), we can get:

$$\begin{aligned} u_p(\omega){u_d}^*(\omega) = \quad & M_0(\omega)[{M_0}^*(\omega) + {M_1}^*(\omega) + {M_2}^*(\omega) + \ldots + {M_n}^*(\omega)] \\ & = [A^0(\omega)P(\omega)P^*(\omega)A^0(\omega)] + [A^0(\omega)P(\omega)P^*(\omega)^2A^1(\omega)] + [A^0(\omega)P(\omega)P^*(\omega)^3A^2(\omega)] \\ & + \ldots + [A^0(\omega)P(\omega)P^*(\omega)^{n+1}A^n(\omega)] \end{aligned} . \quad (21)$$

As mentioned above, when two waveforms with the same propagation path undergo cross-correlation, it can be regarded as canceling the spatial phase, focusing the seismic wave from events into a single point at the origin; therefore, based on the propagation relationship between seismic records, Equation (21) can be further rewritten as:

$$u_p(\omega){u_d}^*(\omega) = [A^0(\omega)A^0(\omega)] + [M_0(\omega)A^1(\omega)] + [M_1(\omega)A^1(\omega)] + \ldots + [M_{n-1}(\omega)A^1(\omega)], \quad (22)$$

For a better understanding of Equation (22), we show the wavefield of seismic interferometry between primaries and multiples in Figure 2. This process can be understood as the deconvolution of multiples. As shown in Figure 2a, the amplitude at 0.5 s represents the primary signal, whereas, in Figure 2b, the peak amplitudes at 1 s and 1.5 s correspond to first-order and second-order multiples, respectively. After interference processing, depicted in Figure 2c, the original primary signal is focused on the origin point (at 0 s), the first-order multiple, which peaks at 1 s, is deconvolved into a primary (peak at 0.5 s), and the second-order multiple is deconvolved into first-order multiple. This means that through this process, we can utilize multiples to enhance the primary signal and obtain new seismic profiles.

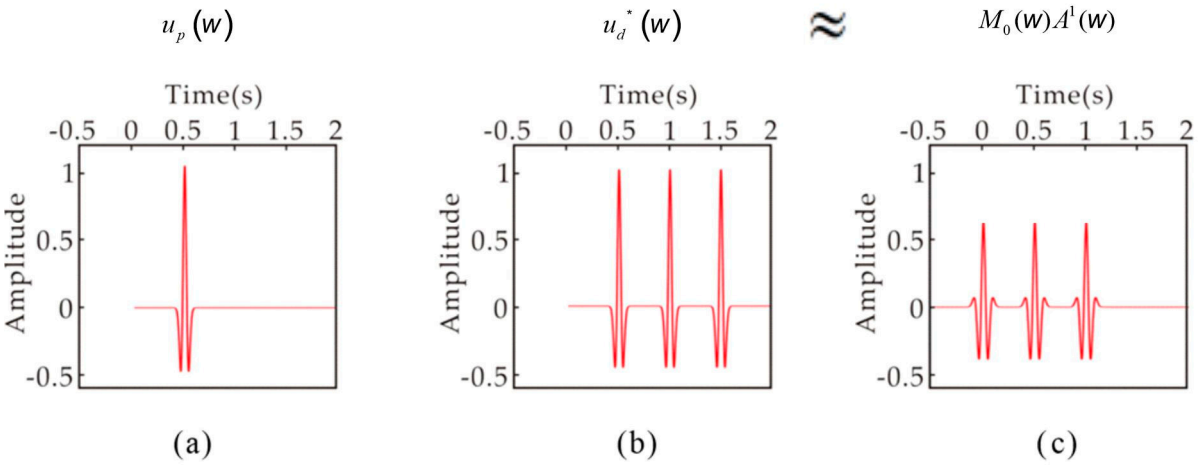


Figure 2. Seismic interferometry using primaries and multiples: (**a**) Primaries; (**b**) Full-wavefield data; (**c**) Processing result.

The full-wavefield formula can be denoted as:

$$u_d(\omega) = M_0(\omega) + M_1(\omega) + M_2(\omega) + \ldots + M_n(\omega), \quad (23)$$

By comparing Equations (22) and (23), it can be observed that the wavefield components of the two show a high degree of similarity. We can consider that through the interference operation between the primary and the full-wavefield data, a wavefield similar to the full-wavefield data can be obtained. Meanwhile, the first-order multiples are downgraded to a quasi-primary wavefield, fully utilizing the wide propagation range and rich information contained in the multiples to supplement the primary information. When

these full-wavefield data contain only the primary and the first-order multiples, we can solve for the particular solution of Equation (25), that is:

$$\begin{aligned} u_p(\omega){u_d}^*(\omega) &= [A^0(\omega)P(\omega)P^*(\omega)A^0(\omega)] + [A^0(\omega)P(\omega)P^*(\omega)^2A^1(\omega)] \\ &= [A^0(\omega)A^0(\omega)] + [M_0(\omega)A^1(\omega)] \end{aligned}, \quad (24)$$

where the data points near the origin can be removed by truncation, so Equation (26) can be approximated as:

$$u_p(\omega){u_d}^*(\omega) \approx M_0(\omega)A^1(\omega), \quad (25)$$

That is, when these full-wavefield data contain only the primary and the first-order multiples, performing seismic interferometry between them can obtain a quasi-primary signal.

2.3. Data Analysis and Pre-Processing for Offshore Wind Farm Data

In this study, we analyzed data from a single-channel seismic survey conducted at an offshore wind farm in the South China Sea. The survey area lies in the southern sea of Fangchenggang, Guangxi, China, approximately 15 km from the nearest coastline (please include a study area map without Chinese annotations). It spans an area of about 99 km^2, with water depths ranging from 0 m to 25 m. This region forms part of a significant Cenozoic sedimentary basin, whose center is located southwest of Weizhou Island. The basin's foundation comprises folded Paleozoic and Mesozoic rocks and sedimentary strata. Data in this study were acquired using an AAE CSP system(manufactured by AAE Technologies, United Kingdom.) with a 700 J electric spark source, and the frequency range is 0.3–1.2 kHz. Shots were spaced every 5 m with a 0.05 ms sampling interval and a total sampling duration of 125 ms. The spark source and hydrophone are deployed at 2.6 m depth and towed 25 m behind to ensure they are away from the wake of the ship.

Offshore wind farm dataset, similar to conventional marine seismic data, is typically compromised by complex noise wavefields [41] from swell, passing vessels, etc. This results in effective signals being heavily masked by noise, which heavily mask effective signals, making them difficult to identify and interpret. As illustrated in Figure 3, these raw data clearly show that after 40 ms, reflection signals are nearly obscured due to strong noise interference. This noise not only challenges data interpretation but also risks misidentification of geological features essential for foundation stability.

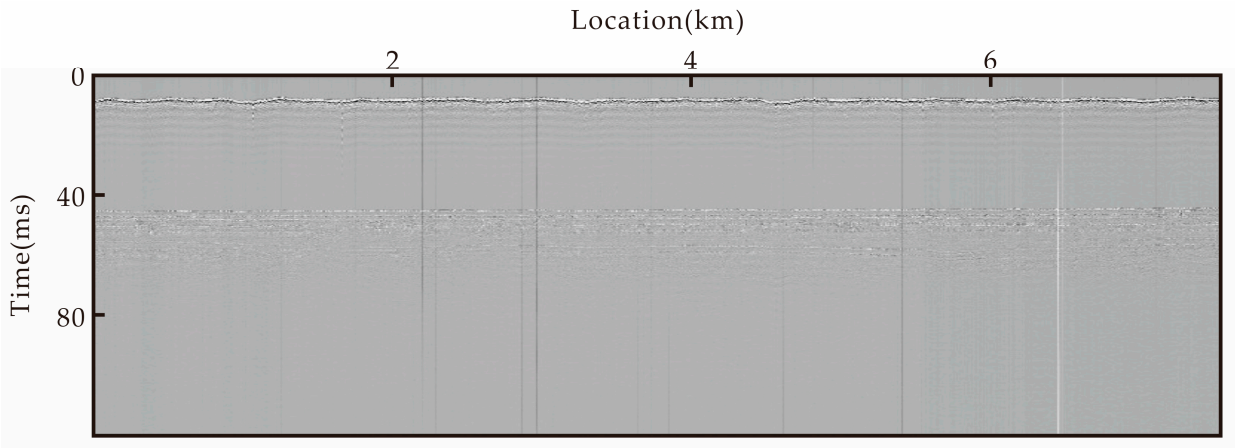


Figure 3. Demonstration of original data from an offshore wind farm.

To improve the reliability of our data analysis, conventional processing steps are initially adopted (Table 1). The main steps include background noise elimination, direct wave removal, swell correction, random noise suppression, and deghosting. Deghosting is crucial in this context, as even the subtle time differences between primaries and ghosts can

significantly degrade the resolution and interpretability of the data. These steps are crucial in enhancing the signal-to-noise ratio, which facilitates the identification of stratigraphic information critical for assessing subsurface medium conditions. Figure 4a shows SCS data profiles with improved signal-to-noise ratios, demonstrating a significant improvement in data quality. This enhancement is crucial for accurately identifying and interpreting, which are vital for assessing the subsurface conditions suitable for wind farm development.

Table 1. Workflow for improving signal-to-noise.

Pre-Process	Noise Attenuation
Mute direct wave	Spectrum analysis
Remove bad channel	Bandpass filtering
Swell correction	Random noise attenuation
	deghosting

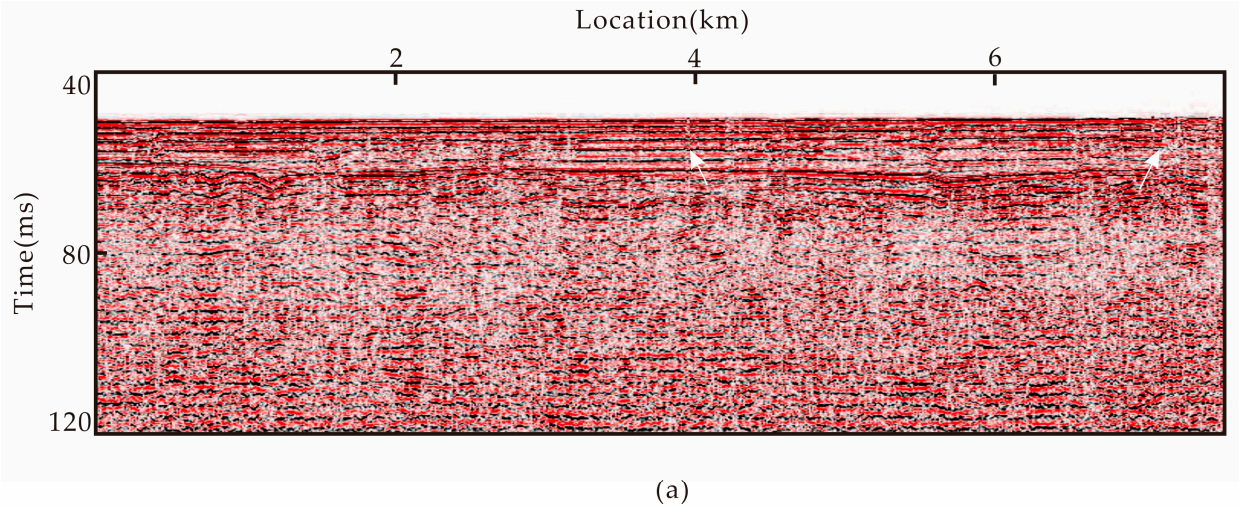


Figure 4. (**a**) Demonstration of data after preprocessing; (**b**) Primary extraction results.

First, our analysis focuses on the wavefield components within these data, which mainly include primary and multiple reflections. Primaries are mainly concentrated in the shallow region from 45 ms to 80 ms, while in the 80 ms to 120 ms region, these data reveal several discontinuous events formed by multiples. These multiples are generated because the sea surface acts as a highly reflective interface, which causes seismic signals that have reflected off the seabed to reflect once more. As a result, multiples are periodic,

travel further than primaries, and are mainly concentrated in the shallow strata, carrying sufficient shallow information. Moreover, we observe two discontinuities at 4 km and 7 km along the survey line (marked by white arrows). These discontinuities complicated local interpretation, making it challenging to discern whether they result from gaps in data acquisition or from actual subsurface structural movements, both of which could significantly influence risk assessments for potential site selection. By addressing these complexities through the subsequent application of seismic interferometry, we aim to improve the clarity and reliability of the subsurface imaging.

Therefore, to obtain interferometric data, we first need to separate the primary signals from the original full-wavefield data. Currently, the most widely used method for primary extraction is the Surface-Related Multiple Elimination (SRME) method [40], which is entirely data-driven and requires no subsurface medium information. By continue processing these full-wavefield data shown in Figure 4a, we can obtain the primary data (shown in Figure 4b). As seen in Figure 4b, in the 80 ms to 120 ms region, the energy of multiples has been effectively suppressed, while the energy of the shallow primaries is well protected. It demonstrates that the application of the SRME method in obtaining primary signals maintains amplitude integrity, laying a foundation for subsequent processing. We use these data, along with the full-wavefield data, as inputs for the seismic interferometry method, enabling us to obtain the interfered data profile. The process can be summarized as follows: the predicted multiples can obtained by convolving and summing the full-wavefield data, which includes both primary and multiple [42]. The multiples are then subtracted from these full-wavefield data to obtain the primary extraction result. This process is represented by the following equation:

$$P(\omega) = \frac{D(\omega)}{\left[1 + r_0 W(S,\omega)^{-1} D(\omega)\right]}, \tag{26}$$

Equation (26) can be defined as surface-related operators A:$A(\omega) = r_0 W(S,\omega)^{-1}$. Consequently, the primary $P(\omega)$ can be expressed in the following series expansion:

$$P(\omega) = D(\omega) - A(\omega)D^2(\omega) + A^2(\omega)D^3(\omega) - \cdots, \tag{27}$$

Furthermore, through an iterative process, we can solve Equation (3) to obtain the primary. The solution process can be represented as follows:

$$P^1(\omega) = D(\omega), \tag{28}$$

$$M^i(\omega) = P^i(\omega)D(\omega), \tag{29}$$

$$P^{i+1}(\omega) = D(\omega) - A(\omega)P^i(\omega)D(\omega). \tag{30}$$

where i is the iterative number.

3. Results

3.1. Comparison Between Different Interferometry Methods for Field SCS Data

Considering that the interferometric results depend on the adequacy of input data, which may be insufficient in SCS data. One of the key issues is to optimize the above three methods. Figure 5 demonstrates, respectively, the interferometry results of the cross-correlation, deconvolution and cross-coherence. Among them, we can see that all the algorithms can reconstruct the main events of primary, which proves the feasibility of multiple-promoting imaging by seismic interferometry.

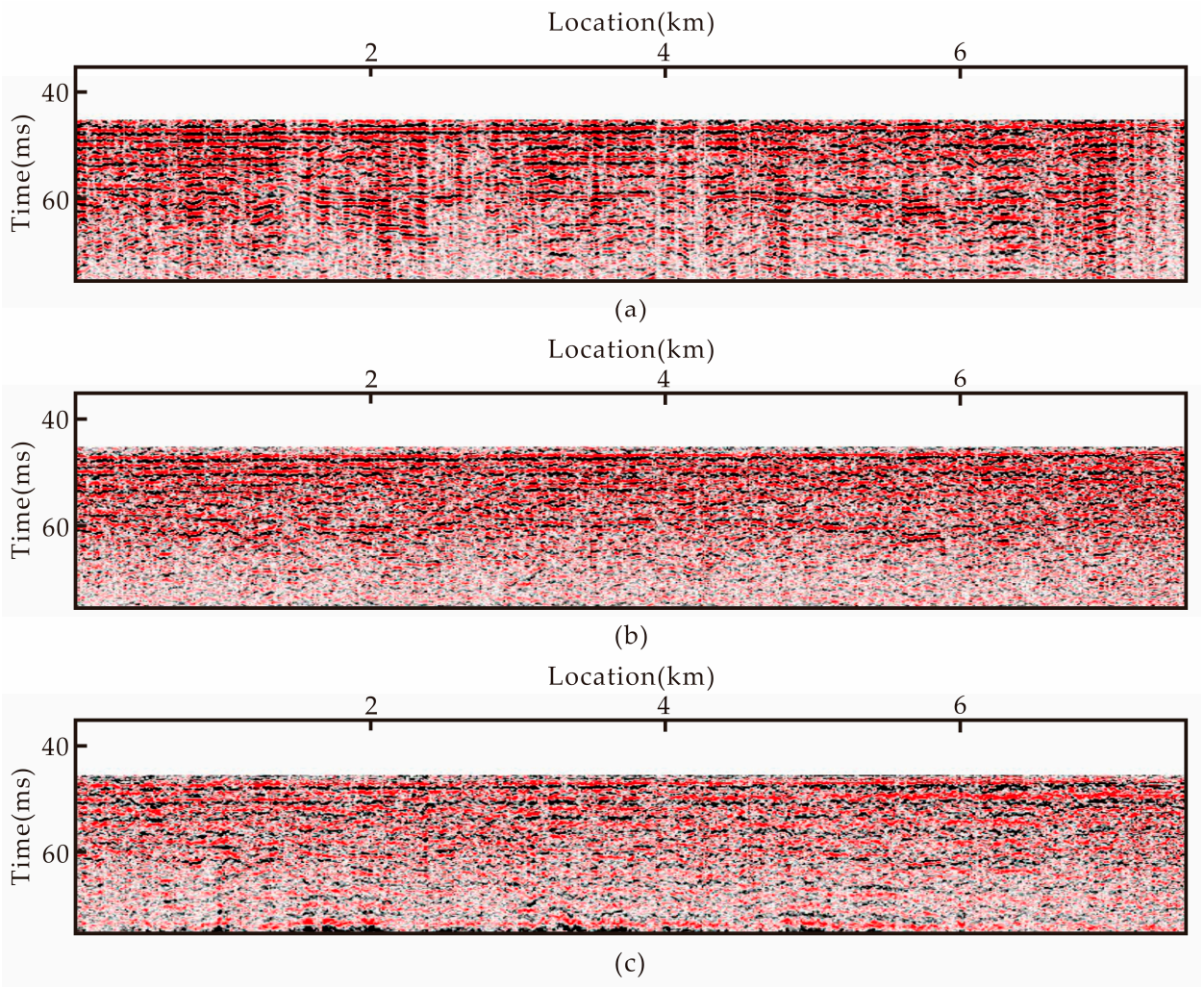


Figure 5. Interferometry results of the three methods: (**a**) Cross-correlation, (**b**) Deconvolution, (**c**) Cross-coherence.

To determine the most suitable interferometry method for offshore wind farm data, we provide a detailed comparison of the results from three different methods: cross-correlation, deconvolution, and cross-coherence. Observing the interferometry results in Figure 5, we can observe significant differences in energy distribution between shallow (45–60 ms) and deep layers (60–75 ms) among these methods. Specifically, the cross-correlation and deconvolution show stronger energy in the shallow layer zone compared with the deep layer zone. In contrast, the cross-coherence shows no notable difference in energy between shallow and deep layers. Moreover, in Figure 5c, which represents the cross-coherence method, we observe strong amplitude artifact strata at deeper positions, which indicates that while the coherence method enhances valid signals, it also amplifies noise, potentially leading to misinterpretations during subsequent interpretation. To verify and quantify this phenomenon, we calculated the energy ratios of the shallow to deep layers for each method, with the results presented in Figure 6. The equation for calculating these ratios is given as [43]:

$$Ratio = \frac{\sum_{t=1}^{t=t_{shallow}} E(t)^2}{\sum_{t=t_{shallow}}^{t=t_{deep}} E(t)^2} \quad (31)$$

where $t_{shallow}$ represents the time index of the shallow layer and t_{deep} represents the time index of the deep layer. In this comparison, we use half of the total sampling time as the boundary between shallow and deep layers. Since the main targets of offshore wind farm assessments are the shallow cover layers prone to geological hazards [36], results with a stronger energy ratio in the shallow layers are qualitatively more suitable for the assessment process. In Figure 6, we find that among the three methods, the deconvolution method achieves the highest overall energy ratio in the shallow layers, with the cross-correlation method slightly inferior, especially in the 5 km to 7.5 km range. In contrast, the coherence method shows the lowest energy ratio in the shallow layers.

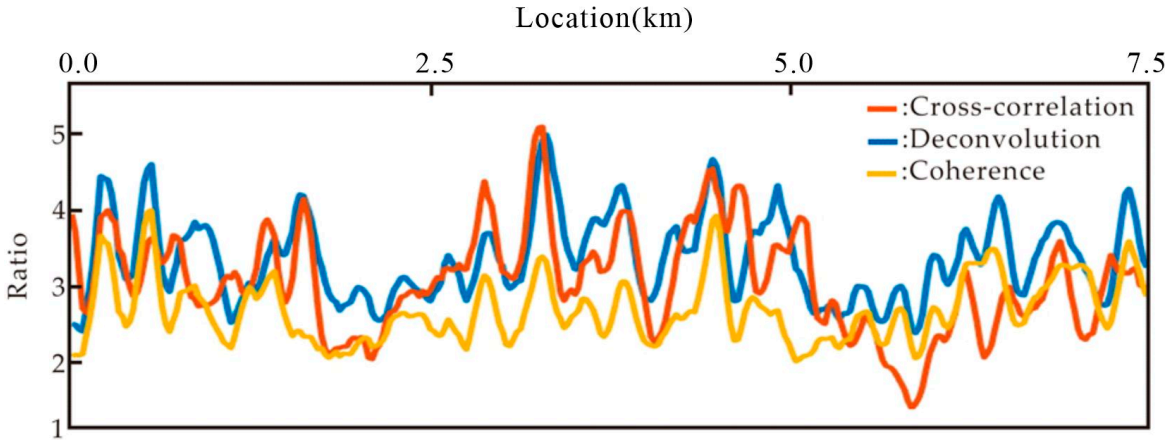


Figure 6. Comparison of energy ratios between shallow and deep layers. The red, blue, and yellow curves represent the cross-correlation, deconvolution, and coherence methods, respectively.

Furthermore, we focus on shallow layer resolution, which is critical for offshore wind farm site assessments. To facilitate a clearer comparison, Figure 7 presents zoomed views of the three datasets. It is evident that the cross-correlation results exhibit significantly more noise and a lower signal-to-noise ratio compared with the deconvolution and coherence algorithms. As a result, only the seabed layer at 47 ms is recognizable in the cross-correlation results, making it difficult to identify additional stratigraphic information. Additionally, the cross-correlation algorithm is influenced by the source wavelet, which fails to adequately attenuate the wavelet phase [38]; the resolution of the stratigraphic layers shown in the cross-correlation results is also lower than the other two algorithms.

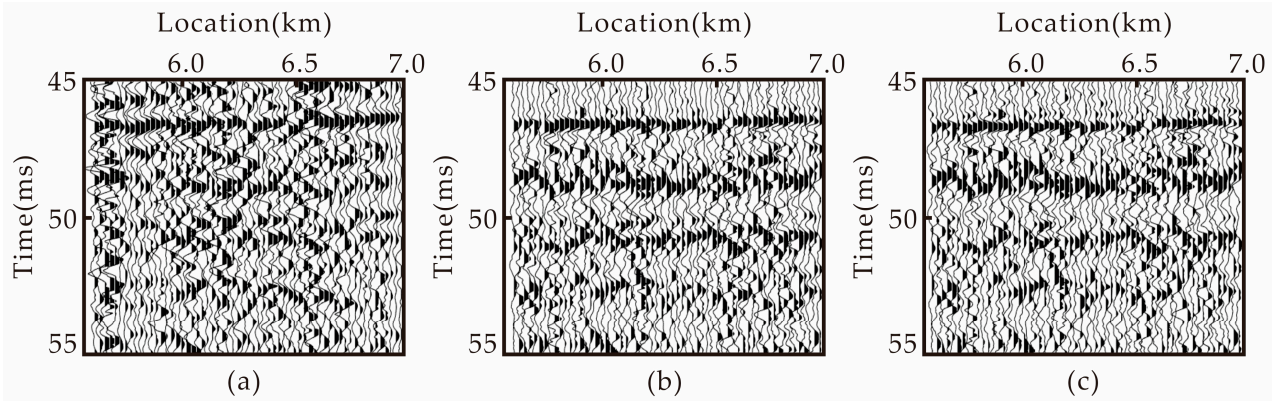


Figure 7. Zoomed-in view of the three Interferometry results: (**a**) Cross-correlation results, (**b**) Deconvolution results, (**c**) Coherence-based results.

Based on the above analysis, we recommend using the deconvolution algorithm for processing offshore wind farm data. Our findings indicate that the cross-correlation algorithm introduces additional noise and results in lower stratum resolution, which may reduce the credibility of data interpretation. Additionally, the cross-coherence algorithm shows limitations in energy distribution, particularly in highlighting shallow target areas. In contrast, the deconvolution method not only overcomes these limitations but also demonstrates significant advantages in amplitude and resolution in shallow layers.

3.2. Comparison of Interferometric Profiles and Conventional Profile

In this section, we compare the optimal deconvolution results with traditional wind farm data profiles to comprehensively evaluate the advantages and disadvantages of interferometric profiles in offshore wind farm applications. Figure 8 shows both the conventional and interferometric profiles, enabling an initial qualitative comparison. Notably, near 47 ms, the discontinuous strata caused by complex acquisition conditions are fixed in the interferometric profile because of the supplement of multiple reflections; however, the interferometric profile introduces some noise, which reduces the signal-to-noise ratio of these data. In the following analysis, we will conduct a more detailed comparison to propose more reasonable processing strategies for offshore wind farm exploration.

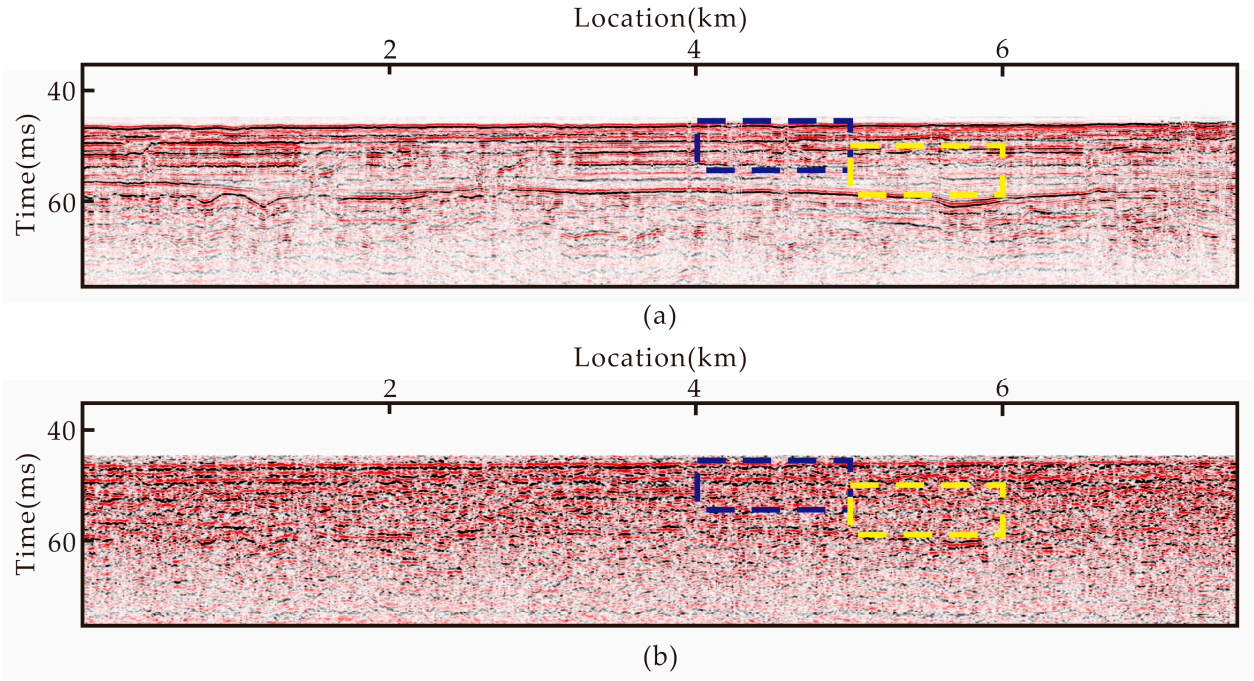


Figure 8. Profile comparison: (**a**) Conventional result; (**b**) Interferometric result.

To better demonstrate the differences in layer resolution between the two profiles, Figures 9 and 10 present a zoomed view of the region highlighted in Figure 8, and we have conducted a corresponding time–frequency analysis (multi-trace average). Comparing the shallow layer results shown in Figure 9, the interferometric profile clearly exhibits higher resolution. Specifically, at 46 ms, the interferometric results display more concentrated energy and a relatively higher amount of high-frequency energy in the time–frequency analysis. Additionally, the conventional profile shows data distortion at the 4.7 km location, whereas the interferometric method corrects these distorted events by utilizing multiple information for data completion, significantly improving stratum continuity.

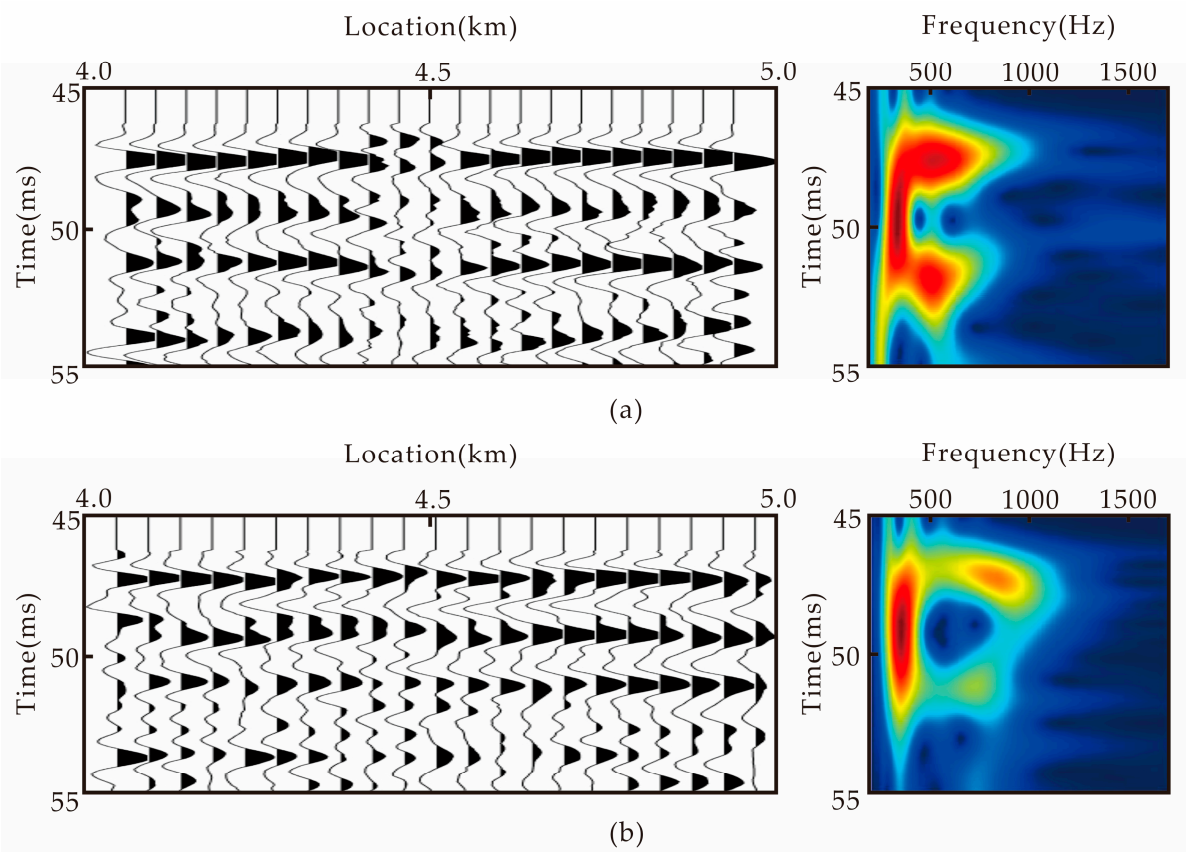


Figure 9. Comparison of zoomed section and time–frequency analysis for the blue box: (**a**) Conventional profile; (**b**) Interferometry profile.

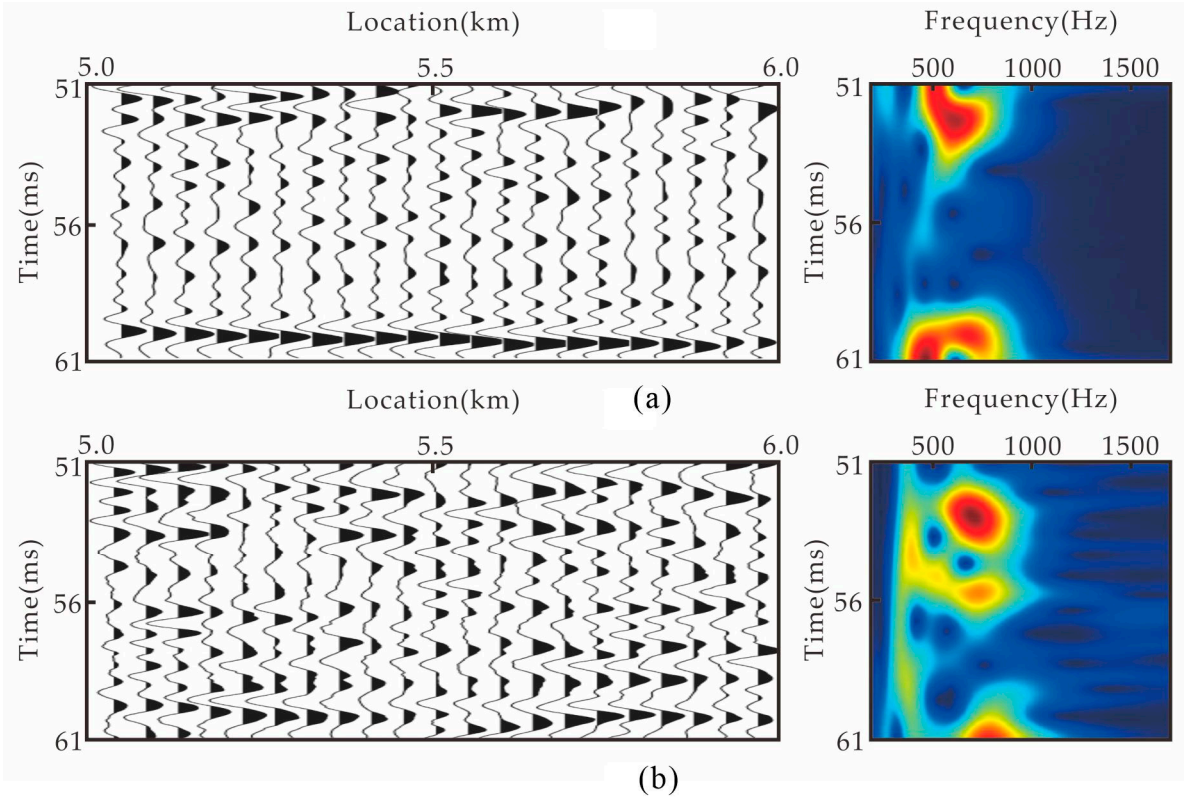


Figure 10. Comparison of zoomed section and time–frequency analysis for the yellow box: (**a**) Conventional profile; (**b**) Interferometry profile.

In the deeper profiles shown in Figure 10, the interferometric method demonstrates superiority in enhancing weak signals. In the 53–58 ms region, layers with weaker energy are difficult to distinguish in the conventional profile due to masking by stronger layers at 53 ms and 58 ms. In contrast, the interferometric profile effectively enhances these weak signals, reducing the risk of overlooking relevant information. Furthermore, the time–frequency analysis in Figure 10a,b confirms the superior resolution of the interferometric method, consistent with the improvements observed in the shallow layers.

However, we should note that the interferometry method introduces new noise into the seismic profiles, thereby decreasing the signal-to-noise ratio. As depth increases, the complexity of seismic wave propagation leads to more mismatches in propagation paths, which introduces noise and increases the difficulty of stratum identification and interpretation.

4. Comprehensive Analysis and Interpretation

Based on our comparative analysis, several key advantages of using interferometric profiles in offshore wind farm site assessments are evident. First, the seismic profiles obtained through interferometry methods offer superior stratum resolution compared with conventional profiles. This enhanced resolution is crucial for precise mapping and analysis of subsurface geological structures, which is pivotal for identifying suitable locations for wind turbine foundations and ensuring their stability. Additionally, seismic interferometry effectively corrects stratum distortions and enhances the energy of weak layers. Correcting distortions is essential for accurately assessing geotechnical risks related to foundation stability, ensuring a more accurate representation of geological conditions vital for the long-term safety and integrity of the wind farm. Enhancing the signals of weak layers is equally important as it helps in identifying less apparent geological features that could influence engineering viability and durability.

However, these methods also have limitations, particularly in introducing additional noise. This increase in noise can reduce the overall signal-to-noise ratio, complicating the identification and interpretation of some layers. Such a reduction in data clarity may lead to challenges in accurately assessing subsurface conditions, potentially affecting the reliability of engineering assessments and wind farm design.

Therefore, we recommend integrating conventional data profiles with interferometric profiles during the offshore wind farm site assessment process to enhance both the precision and reliability of our geological interpretations. In our interpretation process, we primarily rely on the continuity and characteristics of the seismic signals to identify key reflectors indicating stratigraphic boundaries.

Conventional profiles are essential for accurately positioning the general direction of stratum interfaces and overcoming challenges associated with recognizing deeper layers, which might be obscured by excessive noise in interferometric profiles; however, conventional profiles are sometimes limited by data gaps that can lead to stratum distortions, making it difficult to discern the detailed trajectory of reflectors. These uncertainties increase the risk of misidentifying unstable stratum locations, which are crucial for selecting wind farm sites. As a complement, interferometric profiles provide detailed information that enhances the definition and reliability of primary reflectors, particularly due to their advantages in resolution and continuity within shallow layers. We employ semi-automatic picking techniques to map the subsurface features effectively. The accuracy of our interface picks is then corroborated through cross-checks with sidetrack lines and drilling results.

Figure 11 presents the shallow interpreting results of this offshore wind farm data. When interpreting only using the conventional profile (Figure 11a), certain layers with weak energy (indicated by yellow arrows) are difficult to interpret. The main difficulties during

interpretation include (1) lateral discontinuities, making it difficult to determine if they are caused by unstable geological structures, and (2) the presence of short-period interlayer multiples, complicating the identification of the main interfaces. The interferometric profile alone (Figure 11b) benefits from seismic interferometry that eliminates redundant paths and weakens the impact of interlayer multiples, highlighting the primary reflectors. Moreover, the interferometric profile corrected distortions and filled gaps. By combining both profiles, we identified three interfaces in the interferometric profile and matched them to the conventional profile using their travel times (Figure 11c). In total, these profiles provide complementary references for reliable stratigraphic interpretation.

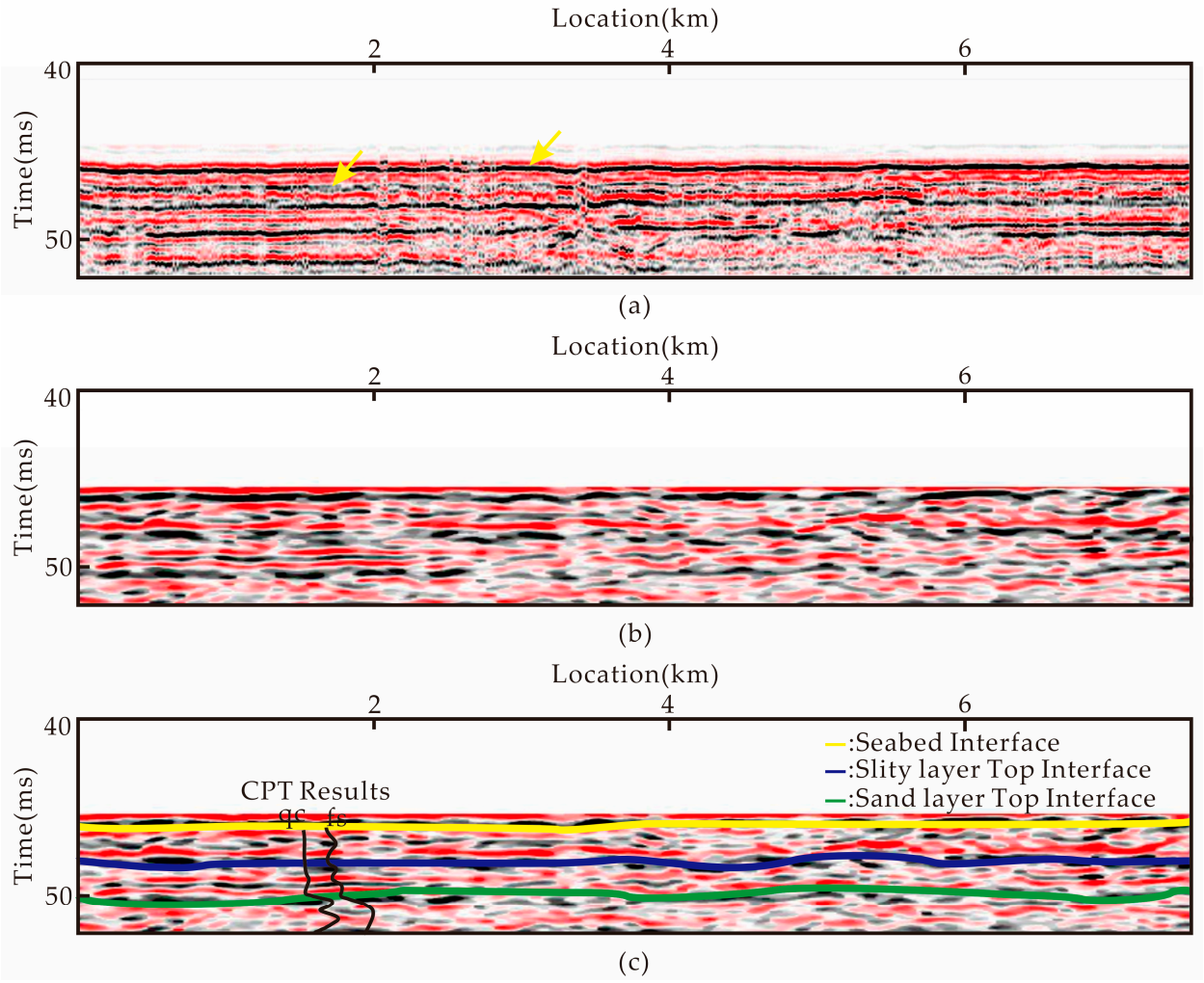


Figure 11. Data interpretation result: (**a**) Conventional profile; (**b**) Interferometry result; (**c**) Interpreted profile.

These drilling data reveal three shallow subsurface layers in the area: a muddy layer, a silty layer, and a sandy layer. These findings align with our interpretation, thereby confirming its accuracy. By comparing Figure 11a,b, it can be observed that it is difficult to determine the positions of the three stratigraphic interfaces on the conventional processing profile, showing poor correlation with drilling data (Table 2) and the Cone Penetration Test (CPT) results (Table 3). In contrast, the interferometric profile presents clear stratification, allowing for accurate identification of the three-layer boundaries, and the profile characteristics align well with the lithological properties obtained from drilling information. As shown in Figure 11b, at the corresponding positions of the CPT curves, we selected two key CPT parameters for plotting the curves: Cone Resistance and Side Friction. Cone

Resistance increases as the rock density increases, which is reflected in the two upward sections of the curve in the figure, each corresponding to the boundary of a new layer. The CPT results are consistent with the SCS result, further supporting the accuracy of our interpretation. Incorporating these drilling data allows for further refinement of seismic profiles. According to these drilling data and CPT results, the silty layer, which includes coarse sand mixed with cohesive soil, silty soil, and angular gravel composed of fine particles, enables minimal energy attenuation of seismic waves, presenting as layered signals (as shown in Figure 11a). In contrast, the layer composed of dense sandstone, conglomerate, and silty clay exhibits distinct properties compared with the sandy layer. Due to its granular composition, the sandy layer induces significant amplitude decay, which is marked by diffuse wave reflections. This leads to a notable loss of energy during wave propagation. This shows that in the larger survey area without a well location, identifying these layer characteristics can provide a good explanation for the survey area. In summary, the joint interpretation of the conventional section and the interference section shows that the strata in the area are relatively flat, and there are no other exposed seismic characteristics, which is suitable for the location of the wind farm.

Table 2. Drilling information from the survey area.

Layer	Layer Description	Profile Features
Muddy layer	Muddy, loose, sandy soil layer	shallowest, continuous stratified reflective layer composed of fine particles, presenting as layered signals characterized by diffuse wave reflections
Silty layer	Loess, angular gravel	
Sand layer	Dense sandy soil, dense loess	

Table 3. Cone Penetration Test (CPT) Results.

Layer	Cone Resistance (qc, MPa)	Side Friction (fs, kPa)	Pore Pressure (u, kPa)	Corrected Cone Resistance (qt, MPa)	Friction Ratio (Rf, %)
Muddy layer	0.09–1.0	2.43–10.27	33.08–270.93	0.10–0.79	0.38–3.12
Silty layer	1.02–1.39	12.13–32.18	299.15–631.26	0.54–1.47	2.24–2.45
Sand layer	6.64–22.02	59.82–66.23	188.52–748.84	3.84–22.11	0.48–3.05

In this paper, we focus on the contribution of seismic interferometry to improving the resolution of seismic profiles for wind farms. To improve the accuracy of the integrated interpretation, future work could explore other processing methods to improve further the clarity and interpretability of the data, such as seismic attribute analysis, including extraction of amplitude, phase, and frequency attributes, which provides the potential for a deeper understanding of the geological conditions. These advanced techniques can significantly improve the resolution and accuracy of seismic interpretation, thereby better-informing engineering decisions for offshore wind farm construction.

5. Conclusions

In this study, we demonstrate the practical application of seismic interferometry in enhancing site assessments for offshore wind farms, highlighting its ability to provide detailed geological structures. By applying various seismic interferometry, notably the deconvolution method, our research significantly improves the resolution and reliability of subsurface imaging. This advancement is crucial for identifying geological structures conducive to wind farm construction. Our method offers a viable alternative to traditional

drilling, presenting a less destructive and more cost-effective strategy for site assessment and facilitating more accurate placement of turbines over extensive areas.

Despite the advancements, the application of seismic interferometry introduces additional challenges, particularly in controlling increased noise levels in processed data. This noise may obscure finer geological details and complicate the interpretation results, potentially affecting the accuracy of the site assessments. Future research should focus on comprehensive interpretation and refining these workflows to minimize noise interference, possibly through the development of advanced filtering algorithms or by enhancing the signal processing workflow.

Author Contributions: All authors made significant contributions to this paper. R.W.: algorithm writing, data analysis, and original manuscript writing. H.Z.: Investigation, development of ideas, and review of the manuscript. P.Z.: data test and review the manuscript. B.H.: Modeling, data test, and manuscript editing. C.L.: Manuscript editing. F.C.: Manuscript checking. All authors have read and agreed to the published version of the manuscript.

Funding: This research was supported in part by the Guangdong Basic and Applied Basic Research Foundation (No. 2023A1515012041), and the Supported by Program for Scientific Research start-up funds of Guangdong Ocean University (No. 06032112311), and the National Key Research and Development Program of China under grant (No. 2022YFC3103101), and the Project of Ocean Research Center of Zhoushan, Zhejiang University (B23107).

Data Availability Statement: Restrictions apply to the datasets. Thedatasets presented in this article are not readily available because the data are part of an ongoing study and technical limitations.

Acknowledgments: We thank the original field datasets and the basic code provided by Deli Wang, Bin Hu, and Junming Zhang of Jilin University.

Conflicts of Interest: All authors declare that the funders had no role in the design of the study, in the collection, analyses, or interpretation of data, in the writing of the manuscript, or in the decision to publish the results.

References

1. Díaz, H.; Soares, C.G. Review of the current status, technology and future trends of offshore wind farms. *Ocean Eng.* **2020**, *209*, 107381. [CrossRef]
2. Bhattacharya, S.; Nikitas, N.; Garnsey, J.; Alexander, N.; Cox, J.; Lombardi, D.; Wood, D.M.; Nash, D.F. Observed dynamic soil–structure interaction in scale testing of offshore wind turbine foundations. *Soil Dyn. Earthq. Eng.* **2013**, *54*, 47–60. [CrossRef]
3. Kaynia, A.M. Seismic considerations in design of offshore wind turbines. *Soil Dyn. Earthq. Eng.* **2019**, *124*, 399–407. [CrossRef]
4. Dinh, V.N.; McKeogh, E. Offshore wind energy: Technology opportunities and challenges. In Proceedings of the 1st Vietnam Symposium on Advances in Offshore Engineering: Energy and Geotechnics, Hanoi, Vietnam, 1–3 November 2018; pp. 3–22.
5. Bashilov, I.P.; Vereshchagin, A.A.; Zagorskiy, L.S.; Zagorskiy, D.L.; Ryazantsev, Y.V.; Chervinchuk, S.Y.; Yudochkin, N.P. Mining Informational and analytical bulletin. *Sci. Tech. J.* **2020**, *12*, 141–150. [CrossRef]
6. Zhou, Q.; Li, X.; Zheng, J.; Li, X.; Kan, G.; Liu, B. Inversion of Sub-Bottom Profile Based on the Sediment Acoustic Empirical Relationship in the Northern South China Sea. *Remote Sens.* **2024**, *16*, 631. [CrossRef]
7. Nasıf, A. Optimal processing of single-channel sparker marine seismic data. *Acta Geophys.* **2024**, *6*, 1–17. [CrossRef]
8. Shareef, N.M.; Mukhopadyay, R.; Sivasamy, A.; Neelakantarama, J.M.; Durga Prasad, P.; Varghese, S. Delineation of buried channels of Bharathappuzha by single-channel shallow seismic survey. *Curr. Sci.* **2016**, *110*, 153.
9. Tsai, L. An Integrated Assessment of Offshore Wind Farm Siting: A Case Study in the Great Lakes of Michigan. Ph.D. Thesis, University of Michigan, Ann Arbor, MI, USA, 2013.
10. Zaaijer, M. Foundation modelling to assess dynamic behaviour of offshore wind turbines. *Appl. Ocean Res.* **2006**, *28*, 45–57. [CrossRef]
11. Chen, Y.; Zhang, M.; Bai, M.; Chen, W. Improving the signal-to-noise ratio of seismological datasets by unsupervised machine learning. *Seismol. Res. Lett.* **2019**, *90*, 1552–1564. [CrossRef]
12. Kearey, P.; Brooks, M.; Hill, I. *An Introduction to Geophysical Exploration*; John Wiley & Sons: Hoboken, NJ, USA, 2002; Volume 4.
13. Telford, W.M.; Geldart, L.P.; Sheriff, R.E. *Applied Geophysics*; Cambridge University Press: Cambridge, UK, 1990.

14. Manshor, N.A.; Amir Hassan, M.H. Seismic geomorphological analysis of channel types: A case study from the Miocene Malay Basin. *J. Geophys. Eng.* **2023**, *20*, 159–171. [CrossRef]
15. Salvação, N.; Guedes Soares, C. Resource assessment methods in the offshore wind energy sector. *Float. Offshore Wind Farms* **2016**, 121–141. [CrossRef]
16. Claerbout, J.F. Synthesis of a layered medium from its acoustic transmission response. *Geophysics* **1968**, *33*, 264–269. [CrossRef]
17. Schuster, G.; Yu, J.; Sheng, J.; Rickett, J. Interferometric/daylight seismic imaging. *Geophys. J. Int.* **2004**, *157*, 838–852. [CrossRef]
18. Draganov, D.; Wapenaar, K.; Thorbecke, J. Seismic interferometry: Reconstructing the earth's reflection response. *Geophysics* **2008**, *71*, SI61–SI70. [CrossRef]
19. Curtis, A.; Halliday, D. Source-receiver wave field interferometry. *Phys. Rev. E—Stat. Nonlinear Soft Matter Phys.* **2010**, *81*, 046601. [CrossRef] [PubMed]
20. Wapenaar, K.; Van Der Neut, J.; Ruigrok, E.; Draganov, D.; Hunziker, J.; Slob, E.; Thorbecke, J.; Snieder, R. Seismic interferometry by crosscorrelation and by multidimensional deconvolution: A systematic comparison. *Geophys. J. Int.* **2011**, *185*, 1335–1364. [CrossRef]
21. Ruigrok, E.; Campman, X.; Draganov, D.; Wapenaar, K. High-resolution lithospheric imaging with seismic interferometry. *Geophys. J. Int.* **2010**, *183*, 339–357. [CrossRef]
22. Huang, H.H.; Lin, F.C.; Tsai, V.C.; Koper, K.D. High-resolution probing of inner core structure with seismic interferometry. *Geophys. Res. Lett.* **2015**, *42*, 10622–10630. [CrossRef]
23. Qiao, B.; Wang, Q.; Lei, Y. Correlation-based interferometry method to enhance near-surface reflection signals in surface active seismic exploration. *IEEE Trans. Geosci. Remote Sens.* **2020**, *59*, 10697–10707. [CrossRef]
24. Fink, C.; Spence, G. Hydrate distribution off Vancouver Island from multifrequency single-channel seismic reflection data. *J. Geophys. Res. Solid Earth* **1999**, *104*, 2909–2922. [CrossRef]
25. Thomsen, K. *Offshore Wind: A Comprehensive Guide to Successful Offshore Wind Farm Installation*; Academic Press: Cambridge, MA, USA, 2014.
26. Feng, X.; Zhang, X.; Liu, C.; Lu, Q. Single-channel and multi-channel orthogonal matching pursuit for seismic trace decomposition. *J. Geophys. Eng.* **2017**, *14*, 90–99. [CrossRef]
27. Boullenger, B.; Draganov, D. Interferometric identification of surface-related multiples. *Geophysics* **2016**, *81*, Q41–Q52. [CrossRef]
28. Guo, B.; Yu, J.; Huang, Y.; Hanafy, S.M.; Schuster, G.T. Benefits and limitations of imaging multiples: Interferometric and resonant migration. *Lead. Edge* **2015**, *34*, 802–805. [CrossRef]
29. Aldawood, A.; Hoteit, I.; Alkhalifah, T. The Linearized Inversion of the Generalized Interferometric Multiple Imaging. In Proceedings of the 2016 SEG International Exposition and Annual Meeting, Dallas, TX, USA, 16–21 October 2016.
30. Neut, J.v.d.; Slob, E.; Wapenaar, K.; Thorbecke, J.; Snieder, R.; Broggini, F. *Interferometric Redatuming of Autofocused Primaries and Internal Multiples*; Society of Exploration Geophysicists: Houston, TX, USA, 2013.
31. Cao, H.; Apatay, E.; Crane, G.; Wu, B.; Gao, K.; Askari, R. Evaluation of Various Data Acquisition Scenarios for the Retrieval of Seismic Body Waves from Ambient Noise Seismic Interferometry Technique via Numerical Modeling. *Geosciences* **2022**, *12*, 270. [CrossRef]
32. Cao, H.; Askari, R. Comparison of seismic interferometry techniques for the retrieval of seismic body waves in CO_2 sequestration monitoring. *J. Geophys. Eng.* **2019**, *16*, 1094–1115. [CrossRef]
33. Xu, Y.; Lebedev, S.; Meier, T.; Bonadio, R.; Bean, C.J. Optimized workflows for high-frequency seismic interferometry using dense arrays. *Geophys. J. Int.* **2021**, *227*, 875–897. [CrossRef]
34. Trampert, J.; Cara, M.; Frogneux, M. SH propagator matrix and Qs estimates from borehole-and surface-recorded earthquake data. *Geophys. J. Int.* **1993**, *112*, 290–299. [CrossRef]
35. Mehta, K.; Snieder, R.; Graizer, V. Downhole receiver function: A case study. *Bull. Seismol. Soc. Am.* **2007**, *97*, 1396–1403. [CrossRef]
36. Aki, K. Space and time spectra of stationary stochastic waves, with special reference to microtremors. *Bull. Earthq. Res. Inst.* **1957**, *35*, 415–456.
37. Prieto, G.; Lawrence, J.; Beroza, G. Anelastic Earth structure from the coherency of the ambient seismic field. *J. Geophys. Res. Solid Earth* **2009**, *114*. [CrossRef]
38. Snieder, R.; Miyazawa, M.; Slob, E.; Vasconcelos, I.; Wapenaar, K. A comparison of strategies for seismic interferometry. *Surv. Geophys.* **2009**, *30*, 503–523. [CrossRef]
39. Mehta, K.; Snieder, R.; Calvert, R.; Sheiman, J. Acquisition geometry requirements for generating virtual-source data. *Lead. Edge* **2008**, *27*, 620–629. [CrossRef]
40. Lai, S.-Y.; Lin, Y.N.; Hsu, H.-H. Efficient 2D multiple attenuation using SRME with curvelet-domain subtraction. *Mar. Geophys. Res.* **2022**, *43*, 1. [CrossRef]
41. Hlebnikov, V.; Elboth, T.; Vinje, V.; Gelius, L.-J. Noise types and their attenuation in towed marine seismic: A tutorial. *Geophysics* **2021**, *86*, W1–W19. [CrossRef]

42. Fang, Y.-F.; Nie, H.-M.; Zhang, L.-M.; Tang, B.-W.; Wang, Z.-B. 3D SRME based on joint regularization and sparse inversion. *Chin. J. Geophys.* **2016**, *59*, 673–681.
43. Yilmaz, Ö. *Seismic Data Analysis: Processing, Inversion, and Interpretation of Seismic Data*; Society of Exploration Geophysicists: Houston, TX, USA, 2001.

Disclaimer/Publisher's Note: The statements, opinions and data contained in all publications are solely those of the individual author(s) and contributor(s) and not of MDPI and/or the editor(s). MDPI and/or the editor(s) disclaim responsibility for any injury to people or property resulting from any ideas, methods, instructions or products referred to in the content.